Chinese Chemical Letters 34 (2023) 108265

Contents lists available at ScienceDirect

Chinese Chemical Letters

journal homepage: www.elsevier.com/locate/cclet

TiO_2 nanorods based self-supported electrode of 1T/2H MoS_2 nanosheets decorated by Ag nano-particles for efficient hydrogen evolution reaction

Changzheng Lin[a], Yunpeng Liu[a], Yaxing Sun[a], Zhenyu Wang[a], Hao Xu[a], Mingtao Li[d], Jiangtao Feng[a,*], Bo Hou[b,*], Wei Yan[a,c,*]

[a] Department of Environmental Science & Engineering, Xi'an Jiaotong University, Xi'an 710049, China
[b] School of Physics and Astronomy, Cardiff University, The Parade, Cardiff, CF24 3AA, Wales, United Kingdom
[c] State Key Laboratory of Multiphase Flow in Power Engineering, Xi'an Jiaotong University, Xi'an 710049, China
[d] International Research Center for Renewable Energy (IRCRE), State Key Laboratory of Multiphase Flow in Power Engineering (MFPE), Xi'an Jiaotong University, Xi'an 710049, China

ARTICLE INFO

Article history:
Received 9 January 2023
Revised 7 February 2023
Accepted 22 February 2023
Available online 26 February 2023

Keywords:
Molybdenum disulfide
Silver nanoparticles
Hydrogen evolution reaction
Density functional theory
Hydrogen spillover

ABSTRACT

Molybdenum disulfide (MoS_2) has shown significant promise as an economic hydrogen evolution reaction (HER) catalyst for hydrogen generation, but its catalytic performance is still lower than noble metal-based catalysists. Herein, a silver nanoparticles (Ag NPs)-decorated 1T/2H phase layered MoS_2 electrocatalyst grown on titanium dioxide nanorod arrays (Ag NPs/1T(2H) MoS_2/TNRs) was prepared through acid-tunable ammonium ion intercalation. Taking advantage of MoS_2 layered structure and crystal phase controllability, as-prepared Ag NPs/1T(2H) MoS_2/TNRs exhibited ultrahigh HER activity. As-proposed strategy combines facile hydrogen desorption (Ag NPs) with efficient hydrogen adsorption (1T/2H MoS_2) effectively circumventes the kinetic limitation of hydrogen desorption by 1T/2H MoS_2. The as-prepared Ag NPs/1T(2H) MoS_2/TNRs electrocatalyst exhibited excellent HER activity in 0.5 mol/L H_2SO_4 with low overpotential (118 mV *vs.* reversible hydrogen electrode (RHE)) and small Tafel slope (38.61 mV/dec). The overpotential exhibts no obvious attenuation after 10 h of constant current flow. First-principles calculation demonstrates that as-prepared 1T/2H MoS_2 exhibit a large capacity to store protons. These protons can be subsequently transferred to Ag NPs, which significantly increases the hydrogen coverage on the surface of Ag NPs in HER process and thus change the rate-determining step of HER on Ag NPs from water dissociation to hydrogen recombination. This study provides a unique strategy to improve the catalytic activity and stability for MoS_2-based electrocatalyst.

Hydrogen is an extremely clean and renewable energy source, which is an ideal substitute of fossil fuels for environmental protection. Among the clean energy conversion methods, hydrogen evolution reaction (HER) is one of the most promising methods for commercial application, which has attracted extensive attentions [1,2]. However, the main obstacle to hydrogen production from water electrolysis is a slow HER and large kinetic hindrance [3]. Platinum (Pt) has been widely studied as an excellent catalyst with extremely high electrical conductivity and excellent hydrogen adsorption and desorption for HER [4–7]. Unfortunately, the broad application of Pt-based catalysts are the significantly limited by their high price and limited natural Pt proven reserves [8]. Thus, the development of Pt-free electrocatalysts with comparable performance, better stability and cost-effectiveness preparation process is imminent.

Researchers have recently investigated many low-cost and high-performance catalysts, mainly including transition metal dichalcogenides (TMDCs) [9–11], metal carbides [12], metal nitrides [13] and metal phosphides [14]. Among these candidates, molybdenum disulfide (MoS_2) has attracted a lot of attention due to its two-dimensional layered structure and abundant catalytic active sites. Due to differences in the structure of layers (1, 2 and 3) and crystals (hexagonal, trigonal and rhombohedral) in a single unit cell, MoS_2 has three natural or synthetic polymorphisms, namely 1-trigonal (1T), 2-hexagonal (2H), and 3-rhombohedral (3R). Unlike 2H-MoS_2 phase, the 1T-MoS_2 phase exhibits metallic prop-

* Corresponding authors.
E-mail addresses: fjtes@xjtu.edu.cn (J. Feng), HouB6@cardiff.ac.uk (B. Hou), yanwei@xjtu.edu.cn (W. Yan).

https://doi.org/10.1016/j.cclet.2023.108265
1001-8417/

erties, so it has a high conductivity facilitating its HER performance [15]. Metastable 1T-MoS_2 can only be obtained under harsh synthetic strategies such as alkali metal intercalation-exfoliation [16,17], doping [18], mechanical strain [19], and electron beam irradiation [20]. However, the yields of the above methods are low, which severely limits the application of 1T-MoS_2. It is a great challenge to obtain high-purity 1T-MoS_2 by a facile method. To address this issue, an acid regulation strategy is employed to efficiently induce phase transition from 2H-MoS_2 to 1T-MoS_2 for enhancing its HER performance [8,21]. To improve the conductivity of MoS_2, the most widely used approache is coating conductive carbon on MoS_2 or loading MoS_2 on conductive carriers to reduce the charge transfer resistance in the electrochemical process [22,23]. Although the high 1T phase MoS_2 catalyst synthesized by the above method improved the HER activity, its stability and surface charge transfer and internal resistance still have great challenges [24,25]. Therefore, it is necessary to develop a new type of MoS_2-based catalyst with a facile growth approach but, high HER performance and stability.

Herein, a novel flower rod-like catalyst stacked by nanosheet MoS_2 was synthesized by hydrothermal grow MoS_2 on the surface of TiO_2 nanorods (TNRs) (Fig. S1a in Supporting information). The organic acid plays a major role in modulating the conversion efficiency of MoS_2 from 2H phase to the 1T phase which promotes electron transfer. Meanwhile, the internal resistance of charge transfer can be reduced by electrodepositing of Ag NPs. The resulting electrocatalyst exhibited excellent HER activity in 0.5 mol/L H_2SO_4 with low overpotential (118 mV *vs.* RHE) and small Tafel slope (38.61 mV/dec). Furthermore, as-prepared Ag NPs/MoS_2/TNRs shows robust cycle stability and there is negligible overpotential attenuation after 10 h of constant current flow.

Fig. S1b and Eq. S1 (Supporting information) show the simple hydrothermal synthesis steps of MoS_2 in H_2O as solvent (H-MoS_2) nanoparticles and MoS_2 nanosheets on TNRs. In this experiment, thiourea as both sulfur source and reductant was employed to promote the formation of molybdenum blue (MB) from Mo-O-Mo bond condensation of protonated Mo-O-Mo under the action of propionic acid. As shown in Fig. S2 (Supporting information), MB species have the typical absorption band around 600–1100 nm which is attributed to the intervalence charge transfer (IVCT) [26]. The maximum absorbance is reached at the propionic acid volume fraction of 58.3 vol%. Fig. S3 (Supporting information) is the Fourier transform infrared spectrometer (FT-IR) spectrum of MB powder, Mo-O bonds with different coordination oxygens have different characteristic absorption bands in the range of 1000–500 cm^{-1} [27]. The band at 1414 cm^{-1} corresponds to the bending vibration of the N–H in ammonium ions (NH_4^+), indicating the presence of NH_4^+ bound to MB through strong electrostatic interaction [28,29]. The result of X-ray photoelectron spectroscopy (XPS) spectrum of the Mo 3d in Fig. S4 (Supporting information) confirms the presence of reduced Mo(V) species in the MB powder. As shown in Fig. S5 (Supporting information), graph element mapping analysis reveals a uniform distribution of Mo, S, C and O elements, further validating the formation of polyoxometalates (POMs) [29]. These data demonstrate that MB was successfully obtained by adding thiourea to sodium molybdate in the mixture of propionic acid and water.

As shown in Fig. 1a, uniformly dense TNRs with an average diameter of 125 ± 5 nm are grown vertically on SnO_2 conductive glass doped with fluorine (FTO) surface. As shown in Fig. 1b, the MoS_2/TNRs show a lamellae MoS_2 intercalated on the TNRs with a diameter of about 400 nm. As shown in Fig. 1c, the electrodeposition of Ag NPs is uniformly loaded on MoS_2/TNRs. Meanwhile, Mo, S, Ti, O and Ag species are detectable and distributed uniformly over the entire sample (Figs. S6 and S7 in Supporting information). Comparing with MoS_2/TNRs, the MoS_2/FTO sample showed

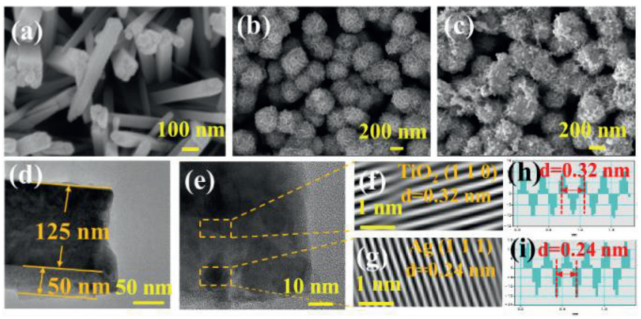

Fig. 1. Top view SEM images of (a) TNRs, (b) MoS_2/TNRs and (c) Ag NPs/MoS_2/TNRs. (d, e) high-resolution TEM (HRTEM) images of Ag NPs/MoS_2/TNRs. The enlarged area denoted in (e) corresponding to the HRTEM images of (f) TiO_2 and (g) Ag, respectively. (h, i) Profile plots of the calibration for measuring the spacings of TiO_2 and Ag.

nanoflower morphology with a diameter of 1.2 μm, but the coverage of MoS_2 was also lower (Figs. S8a and b in Supporting information). MoS_2 on the H-MoS_2/TNRs presents a rod-like stack on the surface of the TNRs, and the layered of MoS_2 has a larger electrochemically active area than the rodlike (Figs. S8c and d in Supporting information). As shown in Fig. 1d, the prepared Ag NPs/MoS_2/TNRs electrodes are composed of TNR with a diameter of about 125 nm and MoS_2 (Ag NPs) with a thickness of 50 nm. The HRTEM (Figs. 1e, f and h) results further confirmed that the as-prepared TiO_2 nanorods possess the (110) plane for rutile TiO_2 [30]. The lattice fringe spacing of 0.24 nm (Figs. 1e, g and i) in the shell corresponds to the (111) plane of Ag NPs [31]. As shown in Fig. S9 (Supporting information), MoS_2 was successfully loaded on TNRs, and Ag element is uniformly distributed on MoS_2. SEM and TEM analysis confirm that the $AgNO_3$ precursor was successfully reduced to Ag NPs by electrodeposition. The close contact between Ag NPs and MoS_2 enables Ag NPs to efficiently transport electrons from Ag NPs to layered MoS_2, which is crucial for the high HER performance of Ag NPs/MoS_2/TNRs electrodes.

As shown in Fig. 2a, the peaks at 3133 and 1400 cm^{-1} are due to the stretching and bending vibrations of the N–H bond, revealing the presence of intercalated NH_4^+ in the MoS_2/TNRs [32]. The XPS spectra of N 1s (Fig. S10 in Supporting information) indicate the presence of intercalated NH_4^+. The Intercalation of NH_4^+ as electron donors lead to the formation and stabilization of 1T-phase MoS_2 [33]. As shown in Fig. 2b, a broad molybdenum sulfide peak is observed only at 13.8° when an aqueous solution of propionic acid was used as the solvent for the hydrothermal preparation of MoS_2 [34]. The Ag NPs peaks in the X-ray diffraction (XRD) pattern of Ag NPs/MoS_2/TNRs are detected at $2\theta = 38.22°$ and 44.35° consistent with (111) and (200) plane (JCPDS card No. 04–0783) [35]. As shown in Fig. 2c, at H-MoS_2/TNRs, the characteristic Raman shifts at 408 and 452 cm^{-1} expected for the $E_{2g}{}^1$ and A_{1g} modes of 2H-MoS_2 are clearly observed [15,36]. At MoS_2/TNRs, the vibration of bridging/shared disulfide ($\nu(S\text{-}S)_{br/sh}$) and terminal disulfide ($\nu(S\text{-}S)_t$) are found at 555 and 525 cm^{-1}, respectively. Molybdenum sulfide bonds [37,38] are found at ν(Mo-S) of 382–284 cm^{-1} whereas the $\nu(Mo_3\text{-}\mu_3S)$ vibration is detected at 450 cm^{-1}. Raman vibration signatures of Ag NPs/MoS_2/TNRs indicate that the disulfide ligands are not displaced after the electrodeposition of silver. As shown in Fig. S11 (Supporting information), H-MoS_2/TNRs, MoS_2/TNRs and Ag NPs/MoS_2/TNRs contain Ag (Ag NPs/MoS_2/TNRs), S, Mo, C and O peaks without any impurity. As can be seen from the curve in Fig. S12 (Supporting information), the high-resolution Mo 3d spectrum of the MoS_2/TNRs sample contains three spin-splitting doublets (Mo $3d_{5/2}$ and Mo $3d_{3/2}$), where Mo $3d_{5/2}$ peaks at ≈228.8 eV, ≈229.5 eV, and ≈233.8 eV. The feature at 228.8 eV and 229.5 eV is assignable to Mo^{4+}, which

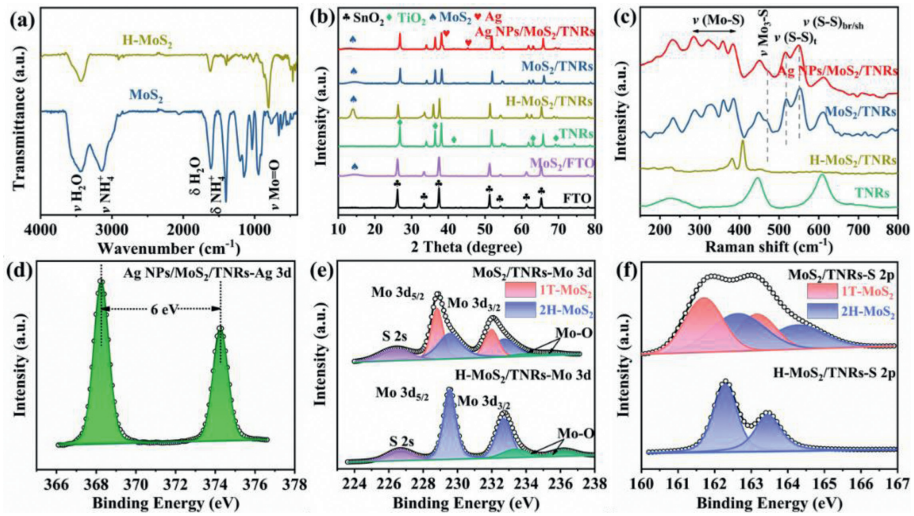

Fig. 2. (a) FT-IR spectra of H-MoS_2 and MoS_2 samples. (b) XRD patterns and (c) Raman spectra of Ag NPs/MoS_2/TNRs and each component. (d) The high-resolution XPS spectra of Ag 3d from Ag NPs/MoS_2/TNRs. The high-resolution XPS spectra of (e) Mo 3d and (f) S 2p from MoS_2/TNRs and H-MoS_2/TNRs.

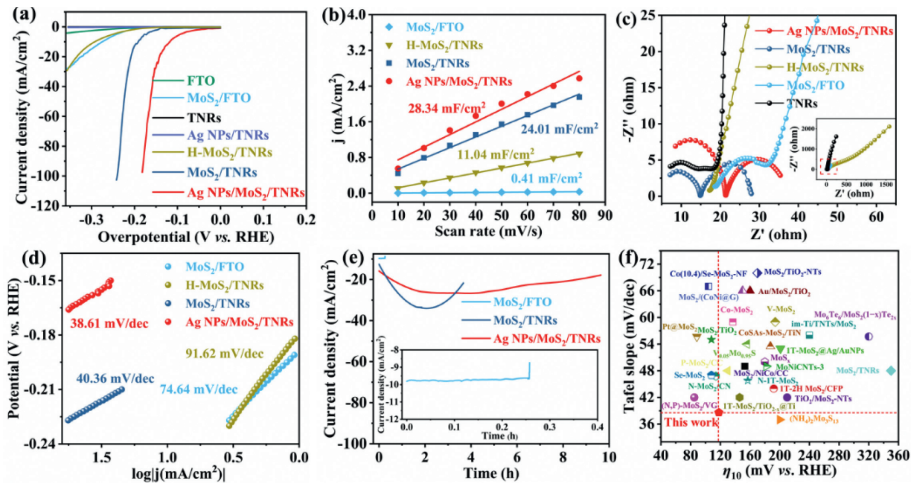

Fig. 3. (a) Polarization curves of electroplating silver in 0.5 mol/L H_2SO_4 solution with a scan rate of 5 mV/s. Capacitive currents with (b) various sweeping velocities, (c) Nyquist plot and (d) tafel plots of the electrodes. (e) Constant voltage response of MoS_2/FTO, MoS_2/TNRs and Ag NPs/MoS_2/TNRs. (f) Comparison Tafel slope and η_{10} with other HER electrocatalysts reported recently. Values were plotted from references (Table S2 in Supporting information).

is compatible with the binding energy of the 1T and 2H phase of MoS_2 [15,31]. Mo^{6+} originates from the MoO_y or MoS_xO_y regions in the electrodes (Figs. S11 and S13 in Supporting information) [39,40]. The high-resolution S 2p spectra in Fig. S14 (Supporting information) further demonstrate the generation of 1T/2H MoS_2. However, these peaks in the MoS_2/TNRs and Ag NPs/MoS_2/TNRs samples are red-shifted. This result proves the existence of electronic interaction between Ag NPs and MoS_2. Furthermore, for the Ag 3d of Ag NPs/MoS_2/TNRs (Fig. 2d), two peaks located at 368.3 eV and 374.3 eV prove the existence of metallic Ag, because the difference between the two peaks is 6.0 eV [41]. In Figs. 2e and f, H-MoS_2/TNRs prepared with water as the only solvent have 2H-MoS_2 but no 1T phase MoS_2. Therefore, XPS results along with electron microscopy, FT-IR, XRD, and Raman demonstrate the successful formation of the acid-controlled ammonium ion intercalated Ag NPs/MoS_2/TNRs hybrid structure with high 1T phase MoS_2 and more active sites.

The experimental results of Figs. S15 and S16 (Supporting information) showed that the overpotential was lowest at a propionic acid volume fraction of 58.3 vol% (Fig. S17 in Supporting information) and 3 mmol/L sodium molybdate and 15 mmol/L thiourea (48 mL solution). Fig. 3a shows that FTO, TNRs and Ag NPs/TNRs hardly exhibit the performance of electrocatalytic hydrogen evolution. Compared with H-MoS_2/TNRs, MoS_2/TNRs have higher electrocatalytic hydrogen evolution performance, which may be due to the high catalytic activity and high electrochemical active area of the 1T phase [15,18,39,42]. After silver electrodeposited, its electrocatalytic hydrogen evolution performance will be further improved, which may be due to electrocatalytic performance and high electrical conductivity of Ag [43]. The electrochemical double-layer capacitance (C_{dl}) value of Ag NPs/MoS_2/TNRs is determined to be 28.34 mF/cm^2, which is 1.2, 2.6 and 69.1 times higher than that of MoS_2/TNRs (24.01 mF/cm^2), H-MoS_2/TNRs (11.04 mF/cm^2) and MoS_2/FTO (0.14 mF/cm^2), respectively (Fig. 3b and Fig. S18 in Supporting information). The maximum C_{dl} value of Ag NPs/MoS_2/TNRs indicates the highest electrochemically active region with exposed active sites, which greatly enhances the HER performance [39]. The Nyquist curve (Fig. 3c) and equivalent circuit fitting (Fig. S19 and Table S1 in Supporting information) results show that MoS_2/FTO and H-MoS_2/TNRs have greater charge transfer resistance ($R_{ct} = 4.83\times10^{11}$ Ω and 6.28×10^{4} Ω) compared with MoS_2/TNRs. These results demonstrate that the crystal phase tuning and Ag NPs deposition can greatly facilitate charge transfer, thereby enhancing the reaction efficiency and promoting efficient

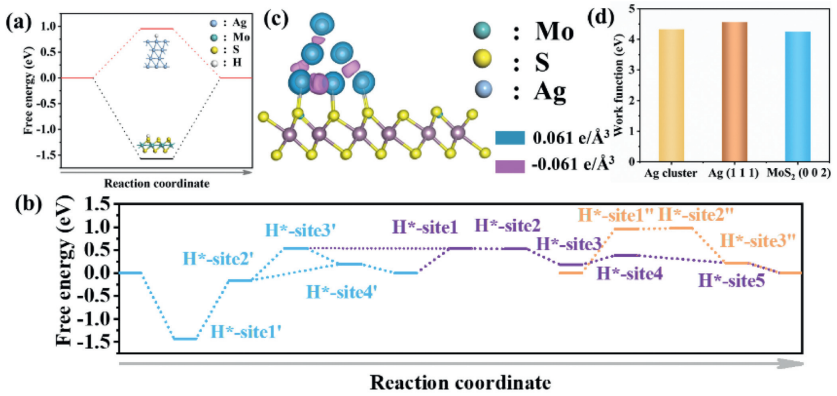

Fig. 4. (a) Calculated free energy diagram for HER on MoS_2 and Ag. (b) Free energies of HER on MoS_2 and Ag were calculated for different hydrogen coverage and adsorption sites. (c) Electron density difference plot across the Ag-MoS_2 interface. Electron accumulation and depletion are indicated in blue and purple, respectively. (d) Work function calculations for various Ag and MoS_2.

electrical integration to reduce parasitic ohmic losses [44,45]. To get into the HER mechanism of these samples, we calculate the Tafel curves based on their linear sweep voltammetry (LSV) (Fig. 3d). The Tafel slope of Ag NPs/MoS_2/TNRs is only 38.61 mV/dec, which is smaller than that of MoS_2/TNRs (40.36 mV/dec), H-MoS_2/TNRs (91.62 mV/dec) and MoS_2/FTO (74.64 mV/dec), indicating that it is more consistent with the Heyrovsky-Tafel mechanism (Eq. S2 in Supporting information). Smaller Tafel slopes show faster HER reaction kinetics, resulting in efficient H_2 generation [42]. The stability of Ag NPs/MoS_2/TNRs, MoS_2/TNRs and MoS_2/FTO are analysed by performing chronoamperometry test (Fig. 3e) at constant potentials (η_{10}) of 120 mV, 210 mV and 280 mV *vs*. RHE, respectively. The presence of TNRs (MoS_2/TNRs) and Ag NPs deposited on MoS_2 surface significantly enhance the stability. As shown in Fig. 3e and Fig. S20 (Supporting information), the polarization curves of Ag NPs/MoS_2/TNRs after 10 h constant voltage test almost overlap, the overpotential at 10 mA/cm^2 changes from the initial 118 mV *vs*. RHE to 123 mV *vs*. RHE, and the overpotential at 50 mA/cm^2 changes from the initial 163 mV *vs*. RHE to 169 mV *vs*. RHE. The above results indicate that TNRs provide good loading sites for MoS_2, which has great advantages over FTO and the enhanced stability of 1T-MoS_2 is related to its substrate and surface electrodeposited Ag NPs. As summerised in Fig. 3f, the HER performance of the as-prepared Ag NPs/MoS_2/TNRs is also better than previous reported Mo-based materials.

Hydrogen spillover, the migration of activated hydrogen atoms generated by the dissociation of di-hydrogen adsorbed on a metal surface onto a reducible metal oxide support, is a common phenomenon in heterogeneous catalysis [3]. To gain theoretical insights into whether hydrogen spillover can take place from MoS_2 to Ag NPs, density functional theory (DFT) calculation was carried out to determine the hydrogen transfer energy barriers. As shown in Fig. 4a, the adsorption of hydrogen is extremely weak on the surface of Ag (111), while the adsorption onto MoS_2 (002) is significantly enhanced, indicating that MoS_2 (002) is prone to hydrogen adsorption. As shown in Fig. 4b and Fig. S21 (Supporting information), the Gibbs free energy (ΔG_{H^*}) of adsorbed hydrogen in MoS_2 surface with the Ag absence (site 1′) tends to be negative. The thermodynamic energy barrier of adsorbed hydrogen desorption to free hydrogen is 0.35 eV, indicating that hydrogen is difficult to desorbed from site 2′ to site 4′. At high hydrogen coverage, the ΔG_{H^*} is 0.54 eV, and the thermodynamic energy barrier with the adsorbed hydrogen on the MoS_2 surface near Ag is 0.2 eV, indicating that the hydrogen transfer process from MoS_2 (site 3′) to MoS_2 near Ag (site 1) is greatly promoted. Additionally, hydrogen adsorption is stronger on Ag NPs (site 4) which is combined to MoS_2 surface, which is more negative at site 4 than at site 1′′. Thus, adsorbed hydrogen can be spontaneously transferred to Ag from the MoS_2 adsorption site covered with high density hydrogen (from site 3′ to site 5). To unravel the facilitated hydrogen transfer process on Ag NPs/MoS_2, the charge density difference was calculated to explore the charge distribution at the interface. As shown in Fig. 4c, electron accumulation is observed below the surface layer of Ag. High density electrons are favorable to trap hydrogen atoms by interacting with unsaturated electrons in the H 1s orbital. As a result, hydrogen spillover from MoS_2 to Ag is thermodynamically and kinetically facilitated. To investigate charge transfer between Ag and MoS_2, the work functions (φ) of Ag and MoS_2 were calculated. The work function of MoS_2 is determined to be 4.25 eV, smaller than that of Ag (4.33 eV), revealing electron transfer from MoS_2 to Ag (Fig. 4d and Fig. S22 in Supporting information). Combining with the above analyses, a reasonable explanation for hydrogen spillover from MoS_2 to Ag is given as follows: the difference in work function between Ag and MoS_2 leads to electron accumulation at the subsurface of Ag, which enhances the hydrogen adsorption on Ag surface and weakens the hydrogen adsorption on the MoS_2 surface, driving the desorption of hydrogen. As shown in Fig. S23 (Supporting information), it is difficult for adsorbed hydrogen on MoS_2 to evolve molecular hydrogen (Pathway 1). As a result, MoS_2 serves as an adsorbed hydrogen reservoir, which form hydrogen through Pathways 2–5.

In conclusion, we proposed a layered 1T/2H phase Ag NPs/MoS_2/TNRs as a high-performance and high-stability electrode for hydrogen evolution in acidic water electrolysis. The composite electrodes have excellent hydrogen evolution performance and low charge transfer resistance. The resulting composite electrodes exhibit good HER activity in 0.5 mol/L H_2SO_4 solution with a low overpotential (118 mV *vs*. RHE) and a small Tafel slope (38.61 mV/dec). More importantly, after electrodeposition of Ag NPs, not only the performance of electrocatalytic hydrogen evolution is increased, but also its stability is significantly increased. These results suggest that Ag NPs, lamellar MoS_2, and TNRs composites have a good synergy effect, which enables each component to play a unique role in efficient-performance of HER applications. DFT simulation and comprehensive characterisations suggest that the high HER catalytic activity of Ag NPs/MoS_2/TNRs in acid possibly results from an unusual hydrogen spillover effect between multiple catalytic sites, whereby MoS_2 site captures proton, then proton diffuses from MoS_2 site to Ag site, and eventually forming H_2 and releases from MoS_2-Ag boundary and Ag site. Our proof-of-concept study of unique molybdenum disulfide supported noble metal structure is expected to be a gen-

eral strategy to improve the catalytic activity and stability of TMDCs.

Declaration of competing interest

The authors declare that they have no known competing financial interests or personal relationships that could have appeared to influence the work reported in this paper.

Acknowledgments

This work was supported by the National Natural Science Foundation of China (No. 52270078) and the Royal Society IEC\NSFC\211201-International Exchanges 2021 Cost Share (NSFC). The authors thank Zijun Ren at the Instrument Analysis Center of Xi'an Jiaotong University for their assistance with SEM analysis

Supplementary materials

Supplementary material associated with this article can be found, in the online version, at doi:10.1016/j.cclet.2023.108265.

References

[1] W. Zhong, X. Wu, Y. Liu, et al., Appl. Catal. B: Environ. 280 (2021) 119455.
[2] Y. Ren, W. Zheng, X. Duan, et al., Environ. Funct. Mater. 1 (2022) 10–20.
[3] J. Chen, C. Chen, M. Qin, et al., Nat. Commun. 13 (2022) 5382.
[4] D. Kobayashi, H. Kobayashi, D. Wu, et al., J. Am. Chem. Soc. 142 (2020) 17250–17254.
[5] D. Zhou, B. Jiang, R. Yang, et al., Chin. Chem. Lett. 31 (2020) 1540–1544.
[6] W. Zheng, Y. Liu, F. Liu, et al., Water Res. 223 (2022) 118994.
[7] C.H. An, W. Kang, Q.B. Deng, et al., Rare Metals 41 (2022) 378–384.
[8] M. Liu, J.A. Wang, W. Klysubun, et al., Nat. Commun. 12 (2021) 5260.
[9] T.L.L. Doan, D.C. Nguyen, S. Prabhakaran, et al., Adv. Funct. Mater. 31 (2021) 2100233.
[10] Y. Xing, N. Li, S. Qiu, et al., Chin. Chem. Lett. 34 (2023) 107724.
[11] T. Guo, L. Wang, S. Sun, et al., Chin. Chem. Lett. 30 (2019) 1253–1260.
[12] X. Li, C. Huang, W. Han, et al., Chin. Chem. Lett. 32 (2021) 2597–2616.
[13] J. Sun, W. Xu, C. Lv, et al., Appl. Catal. B: Environ. 286 (2021) 119882.
[14] C. Pi, C. Huang, Y. Yang, et al., Appl. Catal. B: Environ. 263 (2020) 118358.
[15] X. Chen, Z. Wang, Y. Wei, et al., Angew. Chem. Int. Ed. 58 (2019) 17621–17624.
[16] J. Zheng, H. Zhang, S. Dong, et al., Nat. Commun. 5 (2014) 2995.
[17] Y. Zhao, G. Dong, M. Zhang, et al., 2D Mater. 10 (2023) 014005.
[18] S. Wang, D. Zhang, B. Li, et al., Adv. Energy Mater. 8 (2018) 1801345.
[19] P. Cheng, K. Sun, Y.H. Hu, RSC Adv. 6 (2016) 65691–65697.
[20] Y. Kang, S. Najmaei, Z. Liu, et al., Adv. Mater. 26 (2014) 6467–6471.
[21] Z. Liu, Z. Gao, Y. Liu, et al., ACS Appl. Mater. Interfaces 9 (2017) 25291–25297.
[22] M. Ghosal Chowdhury, L. Sahoo, S. Maity, et al., ACS Appl. Nano Mater. 5 (2022) 7132–7141.
[23] J. Cao, J. Zhou, M. Li, et al., Chin. Chem. Lett. 33 (2022) 3745–3751.
[24] Y. Li, Q. Gu, B. Johannessen, et al., Nano Energy 84 (2021) 105898.
[25] J. Wang, W. Fang, Y. Hu, et al., Catal. Sci. Technol. 10 (2020) 154–163.
[26] I. Nakamura, H.N. Miras, A. Fujiwara, et al., J. Am. Chem. Soc. 137 (2015) 6524–6530.
[27] K.V. Grzhegorzhevskii, P.S. Zelenovskiy, O.V. Koryakova, et al., Inorg. Chim. Acta 489 (2019) 287–300.
[28] P. Yin, B. Wu, T. Li, et al., J. Am. Chem. Soc. 138 (2016) 10623–10629.
[29] S. Lee, J. Hwang, D. Kim, et al., Chem. Eng. J. 419 (2021) 129701.
[30] C. Gao, T. Wei, Y. Zhang, et al., Adv. Mater. 31 (2019) 1806596.
[31] W. Zou, Z. Liu, R. Li, et al., J. Hazard. Mater. 416 (2021) 126043.
[32] X.H. Lin, X.J. Yin, J.Y. Liu, et al., Appl. Catal. B: Environ. 203 (2017) 731–739.
[33] D. Wang, Y. Xiao, X. Luo, et al., ACS Sustain. Chem. Eng. 5 (2017) 2509–2515.
[34] F. Xi, P. Bogdanoff, K. Harbauer, et al., ACS Catal. 9 (2019) 2368–2380.
[35] M. Tahir, B. Tahir, N.A.S. Amin, Appl. Catal. B: Environ. 204 (2017) 548–560.
[36] M.A. Lukowski, A.S. Daniel, F. Meng, et al., J. Am. Chem. Soc. 135 (2013) 10274–10277.
[37] P.D. Tran, T.V. Tran, M. Orio, et al., Nat. Mater. 15 (2016) 640–646.
[38] Y. Wu, J. Wang, Y. Li, et al., Nat. Commun. 13 (2022) 3008.
[39] X. Li, X. Lv, X. Sun, et al., Appl. Catal. B: Environ. 284 (2021) 119708.
[40] M. Li, B. Cai, R. Tian, et al., Chem. Eng. J. 409 (2021) 128158.
[41] T. Zhao, Z. Xing, Z. Xiu, et al., J. Hazard. Mater. 364 (2019) 117–124.
[42] T. Zhang, T. Yang, G. Qu, et al., J. Energy Chem. 68 (2022) 71–77.
[43] J. Chen, G. Liu, Y. Zhu, et al., J. Am. Chem. Soc. 142 (2020) 7161–7167.
[44] X. Wang, Y. Zhang, H. Si, et al., J. Am. Chem. Soc. 142 (2020) 4298–4308.
[45] Z. Luo, Y. Ouyang, H. Zhang, et al., Nat. Commun. 9 (2018) 2120.